## Original article

# Numerical study of response behaviors of natural gas hydrate reservoir around wellbore induced by water jet slotting

Man Huang[1,2], Dongchao Su[1,2], Zhirui Zhao[1,2], Lianghong Wu[1,2], Bin Fang[3], Fulong Ning[1,2]*

[1]*Faculty of Engineering, China University of Geosciences, Wuhan 430074, P. R. China*
[2]*Engineering Research Center of Rock-Soil Drilling & Excavation and Protection, Ministry of Education, Wuhan 430072, P. R. China*
[3]*Process and Energy Department, Delft University of Technology, Delft 2628CB, The Netherlands*

**Abstract:**
The trial production of natural gas hydrate reservoirs remains poor. Reasonable reservoir reconstruction, which can improve formation permeability, is an important approach to increasing the efficiency and enhancing production. In this work, water jet slotting is proposed to reconstruct an natural gas hydrate reservoir near a wellbore. The spatial slots formed by water jet slotting not only directly constitute high-permeability channels, but also generate disturbances to the surrounding in-situ sediment. Water jet slotting disturbances to nearby sediment was investigated using a three dimensional flow-structure coupling model to evaluate the proposed reconstruction method. The reservoir at the SH2 site in the Shenhu area of the South China Sea was used as the reference. A horizontal slotting arrangement along the vertical well was adopted. The results demonstrate that water jet slotting can change the primary stress state of the sediment around the wellbore, and generate a dominant stress relaxation zone and small stress concentration zone. Within the stress relaxation zone, the in-situ compressive stress was remarkably reduced or even transformed into tensile stress, accompanied by sediment displacement and volumetric expansion strain. This is conducive to loosening the sediment around the wellbore and improving the permeability characteristics. In addition, the influence of the water jet slotting parameters including slot radius, spacing, and number on disturbances to the nearby sediment was studied. Reservoir responses to water jet slotting under balanced and unbalanced bottom-hole pressures were compared and analyzed. This study provides a reference for natural gas hydrate reservoir reconstruction using water jet slotting.

## 1. Introduction

Natural gas hydrate (NGH) is an ice-like cage crystalline substance formed by natural gas and water molecules at high pressure and low temperature, and is commonly known as combustible ice. In the 1960s, NGH was found in nature and was considered a potential alternative energy source (Makogon, 1965). Subsequently, the United States, Japan, and China have implemented a series of NGH research and development plans (Liu and Li, 2021). More than 230 NGH occurrence areas have been detected in coastal slopes, polar regions, and permafrost zones (Makogon, 2010; Liu and Li, 2021; Wu et al., 2022), with estimated total reserves reaching 3,000-20,000 trillion cubic meters, twice that of traditional fossil fuels (Yin et al., 2019). The total reserves of NGH in China are estimated to be approximately 84 trillion cubic meters; the prospective NGH resources on the northern slope of the South China Sea (SCS) alone amount to tens of billions of tons of oil equivalent (Liang et al., 2020). The industrialized development of NGH has a significant potential for improving the energy consumption structure, ensuring national energy security, and realizing the two-carbon strategic goal.

The essential principle of NGH exploitation is to break the in-situ stable conditions to promote decomposition and then discharge natural gas. Thus, mining methods such as depressurization, heat stimulation, inhibitor injection, and $CO_2$

replacement are being developed (Cui et al., 2018; Liang et al., 2020). In addition, there is also a solid fluidization method, wherein NGH is collected by water jet crushing (Zhou et al., 2018). To date, eleven NGH trial productions have been undertaken worldwide (Kurihara et al., 2010; Yamamoto et al., 2014; Chen et al., 2018; Yamamoto et al., 2019; Ye et al., 2020), including seven depressurizations, one heat stimulation, one combined depressurization-thermal method, one combined depressurization-replacement method, and one solid fluidization. In 2020, a second trial production was initiated in the Shenhu area of the SCS. A horizontal well was adopted and achieved a historical breakthrough of continuous gas production for 30 days, a total gas production of 860,000 cubic meters, and an average gas production of 29,000 cubic meters per day (Ye et al., 2020).

In the past 30 years, the research and development of NGH has made outstanding achievements. However, there remains considerable work to be done before commercial exploitation can occur. The greatest challenge in NGH industrialization is the low mining efficiency and high safety risk (Liu et al., 2017; Yang et al., 2017; Li et al., 2021a; Shaibu et al., 2021). The establishment of the theory and technical systems of NGH reservoir reconstruction to improve reservoir permeability and mechanical stability to increase efficiency and enhance production is critical (Cai et al., 2020a, 2020b; Wu et al., 2021). In addition, the successful exploitation mode of shale gas with a horizontal well and hydraulic fracturing provides beneficial experiences for NGH exploitation (Wanniarachchi et al., 2017). Therefore, based on previous studies of NGH reservoir characteristics, researchers have mainly investigated three aspects of reservoir reconstruction: hydraulic fracturing, near-well reconstruction, and chemical stimulation.

NGH reservoir hydraulic fracturing has made rapid progress in fracturing tests, crack initiation and propagation simulations, and post-fracturing gas production evaluations. Specifically, hydraulic fracturing tests have been conducted on NGH-free sediment (Khodaverdian and Mcelfresh, 2000; Ito et al., 2008; Lu et al., 2021), NGH-containing sandy sediment (Konno et al., 2016; Too et al., 2018a, 2018b; Zhang et al., 2020), and NGH-containing clay silt sediment (Yang et al., 2020; Sun et al., 2021). All samples demonstrated acceptable fracturability. The fracturing in NGH-free sediment depends on fluid invasion and shear failure in front of the crack tip, whereas the mechanism in NGH-containing sediment is similar to that in conventional rock, namely, tensile failure mode (Khodaverdian and Mcelfresh, 2000). In crack initiation and propagation simulations, the "cohesive unit" model (Ma et al., 2021a) and PFC2D model (Yao et al., 2021) have been established. The "cohesive unit" model couples the physical mechanisms of crack initiation, crack propagation, fluid flow, fluid filtration, and matrix deformation (Ma et al., 2021a), and has been used to study the behavior of single cluster fracturing, synchronous fracturing, and sequential fracturing of an NGH reservoir at the SH2 station in the Shenhu sea area. The PFC2D fracturing model is composed of medium particles, the contact relationships between the particles, and the fluid flow part, which can describe shear and tensile failure (Yao et al., 2021). The simulations indicate that NGH saturation

and the occurrence mode have an important influence on fracturing behavior. Furthermore, the effect of fracturing on gas production has been investigated using numerical tools such as Tough+Hydrate. The production performance of vertical wells (Chen et al., 2017; Feng et al., 2019; Guo et al., 2020; Li et al., 2021b), horizontal wells (Sun et al., 2019; Ma et al., 2021b; Shen et al., 2021; Yu et al., 2021), and three-well injection-production systems (Ju et al., 2020; Zhong et al., 2020, 2021) in NGH reservoirs after fracturing has been numerically studied. Gas production has also been analyzed for laboratory scale fracturing (Feng et al., 2021; Zhao et al., 2021). Overall, high-permeability artificial fractures can improve the effects of depressurization and heat injection, facilitate gas-water seepage, and enhance production performance.

In addition to hydraulic fracturing, methods for near-well reconstruction and chemical stimulation have been proposed and studied. Near-well reconstruction methods include jet grouting slots, grouting columns around wells, and stratified split grouting (Li et al., 2020a, 2020b; Yuan et al., 2021; Yun et al., 2021). The simulation data illustrate that under certain conditions, jet-grouting-slot wellbores can increase productivity by approximately three times compared with open-hole completion (Li et al., 2020b). The most significant production enhancement occurs when grouting slots are located in the three-phase layer (Yun et al., 2021). Under the research conditions, the grouting column around a well with a radius of 0.5 m can improve the hydrate decomposition efficiency by 157%, cumulative gas production by 110%, and average gas-water ratio by 31% (Yuan et al., 2021). The stimulation effect depends primarily on the radius and height of the grouting column. Stratified split grouting not only promotes the expansion of low pressure and improves production performance, but also has a role in strengthening mechanical stability (Li et al., 2020a). The chemical stimulation of methanol huff and puff has proved it effective in increasing the output, as proven by numerical simulations (Masuda et al., 2008).

Previous investigations have provided an acceptable theoretical basis and technical guidance for NGH reservoir reconstruction. Herein, we propose a new method for reconstructing the reservoir around a wellbore using water jet slotting (WJS). Unlike existing jet grouting slots and grouting columns around a well (Li et al., 2020b; Yuan et al., 2021), WJS does not use cement slurry and has no grouting procedure through a long drill string. Therefore, the technological process of WJS is simpler and easier to operate. In this study, a three dimensional (3D) flow-structure coupling model is established to evaluate the proposed WJS method for reconstructing an NGH reservoir. An NGH reservoir in the Shenhu sea area was used as the geological reference. Horizontal slots along vertical-well mode was adopted. The mechanical response behavior of the sediment around the wellbore to WJS reconstruction were analyzed. The slotting-parameter sensitivity on the reconstruction effect was investigated in detail. The current study provides an innovative option for improving sediment permeability near wellbores, with the expectation of promoting the efficient exploitation of NGH reservoirs.
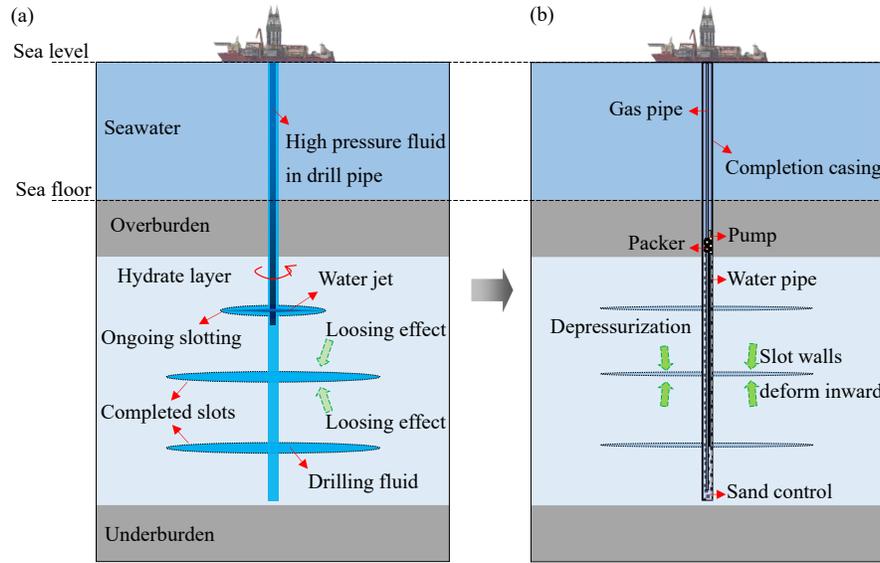
**Fig. 1**. Schematic diagram of reconstructing NGH reservoir by WJS. (a) Water jet slotting and (b) Casing completion and production.

## 2. Completion of WJS in marine sediment

As displayed in Fig. 1, first, a high-speed water jet is used to cut the near-well formation to generate the slot space. Under in-situ stress, the reservoir sediment around the slot squeezes towards the slot space. Correspondingly, the effective stress in the sediment near the slots tends to decrease, resulting in a loosening effect, which is conducive to porosity and permeability improvement. Then, commonly used casing and perforation are employed for completion. It should be noted that the slot itself is a high-permeability channel, and the loosening effect caused by the free slot walls enlarges the influence range of the reservoir reconstruction. These are propitious for subsequent production. Moreover, the perforated casing can ensure wellbore stability during production.

## 3. Model description

### 3.1 Model assumptions

The major objective of this work is to investigate the response behavior of NGH reservoirs around wellbores induced by WJS. The numerical model was established with reference to the NGH reservoir in the Shenhu area, which was idealized to be composed of an overburden layer, overburden layer, NGH sediment strata, vertical production well, and multiple slots. A slot was simplified as a disc-shaped space with a certain thickness, although the slot shape could be complicated owing to different factors in practical slotting operations. Considering the emphasis on the sediment responses, basic assumptions were made to establish the fluid-structure coupling mathematical model:

1) all layers were simplified as an equivalent continuous porous medium with homogeneous and isotropic properties;
2) the flow followed Darcy's law and the deformation

obeyed elasticity;
3) NGH decomposition and formation were not considered;
4) the reservoir was saturated with single-phase water;
5) the pore pressure followed a hydrostatic distribution.

### 3.2 Governing equations

#### 3.2.1 Fluid-structure coupling

The constitutive relation of fluid-structure coupling (Terzaghi, 1943) is:

$$\sigma = C\varepsilon - \alpha_B p_f I \tag{1}$$

where $\sigma$ is the Cauchy stress tensor, Pa; $C$ is the elasticity matrix; $\varepsilon$ is the strain tensor; $\alpha_B$ is the Biot-Willis coefficient; $p_f$ is the fluid pore pressure, Pa; and $I$ is the unit matrix.

Eq. (1) can be divided into volumetric and deviatoric parts. The volumetric part contains the coupling, which is written as:

$$p_m = -k_d \varepsilon_v + \alpha_B p_f \tag{2}$$

where $p_m$ is the mean pressure calculated from the stress tensor $\sigma$, Pa; $K_d$ is the bulk modulus of the drained porous sediment, Pa; and $\varepsilon_v$ is the volumetric strain.

The deviatoric part is independent of the pore pressure coupling and is written as:

$$\text{dev}(\sigma) = 2G_d \text{dev}(\varepsilon) \tag{3}$$

where $G_d$ is the shear modulus of the drained porous sediment, Pa.

Based on Biot's theory (Biot, 1962), the constitutive relation relating the increment in fluid content $\eta$, volumetric strain, and incremental pore pressure is written as:

$$p_f = \frac{1}{S}(\eta - \alpha_B \varepsilon_v) \tag{4}$$

where $S$ is the storage coefficient, Pa$^{-1}$. It is defined as the

change in $\eta$ due to $p_f$ under constant $\varepsilon_v$, and can be calculated from the basic material properties as:

$$S = \frac{\phi}{K_f} + (\alpha_B - \phi)\frac{1 - \alpha_B}{K_d} \qquad (5)$$

where $\phi$ is the porosity and $K_f$ is the fluid bulk modulus, Pa. For a soft porous sediment, $\alpha_B \approx 1$ and $S \approx \phi/K_f$.

### 3.2.2 Fluid flow

The continuity equation is:

$$\frac{\partial}{\partial t}(\rho_f \phi) + \nabla \cdot (\rho_f u) = Q_m \qquad (6)$$

where $\rho_f$ is the fluid density, kg/m$^3$; $u$ is Darcy's velocity, m/s; and $Q_m$ is the source term, kg/(m$^3$·s).

Darcy's velocity reads:

$$u = -\frac{k}{\mu}\left(\nabla p_f + \rho_f g \nabla H\right) \qquad (7)$$

where $k$ is the sediment permeability, m$^2$; $\mu$ is the fluid dynamic viscosity, Pa·s; $g$ is the acceleration of gravity, m/s$^2$; and $H$ is the height, m.

The storage model is:

$$\frac{\partial}{\partial t}(\rho_f \phi) = \rho_f S \frac{\partial p_f}{\partial t} \qquad (8)$$

The source term can be written as:

$$Q_m = -\rho_f \alpha_B \frac{\partial \phi}{\partial t} \qquad (9)$$

### 3.2.3 Solid deformation

Based on Navier's theory (Truesdell, 1972), the equilibrium of sediment under a purely gravitational load is:

$$\nabla \cdot \sigma + (p_f \phi + \rho_s) g = 0 \qquad (10)$$

where $\rho_s$ is the density of the drained sediment density, kg/m$^3$. It is worth noting that the fluid-structure coupling enters as an additional volumetric part in the stress tensor. Specifically, the value of $\sigma$ in Eq. (10) includes two parts: volumetric and deviatoric. The pore pressure $p_f$ acts primarily on the volumetric part, as described in Eq. (2).

## 3.3 Model verification

The above governing equations comprise the mathematical model for the fluid flow to sediment deformation coupling processes in an NGH reservoir. The finite element method was adopted to solve the partial differential equations. Before further investigation, it was necessary to verify the reliability of the established model. Nevertheless, owing to the lack of experimental data on the fluid-structure coupling in NGH-bearing sediment, the fluid flow and solid deformation of the proposed model were verified by an analytical solution and triaxial test data, respectively.

### 3.3.1 Porous seepage verification

A simple saturated seepage problem was employed to verify the fluid flow module. The parameters are listed in Table 1. An analytical solution was used to calculate the pore pre-

**Table 1**. Key parameters in seepage case (Feng et al., 2014).

| Parameters | Values |
|---|---|
| Model size (m) | $100 \times 1$ |
| Pressure on the left (Pa) | $1.0 \times 10^4$ |
| Pressure on the right (Pa) | 0 |
| Fluid density (kg/m$^3$) | 1000 |
| Bulk modulus (Pa) | $1.0 \times 10^{-9}$ |
| Porosity | 0.1 |
| Initial saturation | 1.0 |
| Permeability (m$^2$) | $1.0 \times 10^{-15}$ |
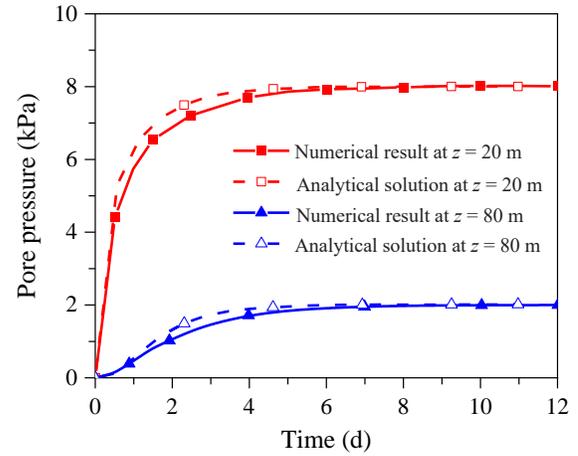


**Fig. 2**. Comparison between numerical and analytical solutions of seepage problem.

ssure in the porous medium (Feng et al., 2014), as given by Eq. (11). Conversely, the seepage problem was described and solved by the presented numerical method. The pore pressures at $z = 20$ and 80 m within a 12-day flow period were monitored. The analytical and numerical solutions are compared in Fig. 2. It can be concluded that the numerical data and analytical solution are in acceptable agreement, particularly when the flow achieves a steady state:

$$\overline{p}(\overline{z}, t) = 1 - \overline{z} - \frac{2}{\pi}\sum_{n=1}^{\infty} e^{-n^2\pi^2 \overline{t}}\frac{\sin(n\pi\overline{z})}{n} \qquad (11)$$

where $\overline{p} = p/p_1$, $\overline{z} = z/L$, $\overline{t} = ct/L^2$, $c = M\rho_f kg/\mu$, $M = K_f/n$; $t$ is the time step, s; $z$ is the distance from the left boundary, m; $L$ is the computed domain length, m; $K_f$ represents the fluid's bulk modulus, Pa; $M$ is the Biot modulus of the porous media; and $n$ is a positive integer.

### 3.3.2 Sediment deformation verification

Triaxial test data from NGH-bearing sediment samples were used to verify the structural module (Ebinuma et al., 2005; Klar et al., 2005; Klar et al., 2010). The sample parameters are listed in Table 2. The NGH saturation values were 0, 10%, 44%, and 53%. The effective confining pressure was 3 MPa. Referring to the experiment, numerical simulations
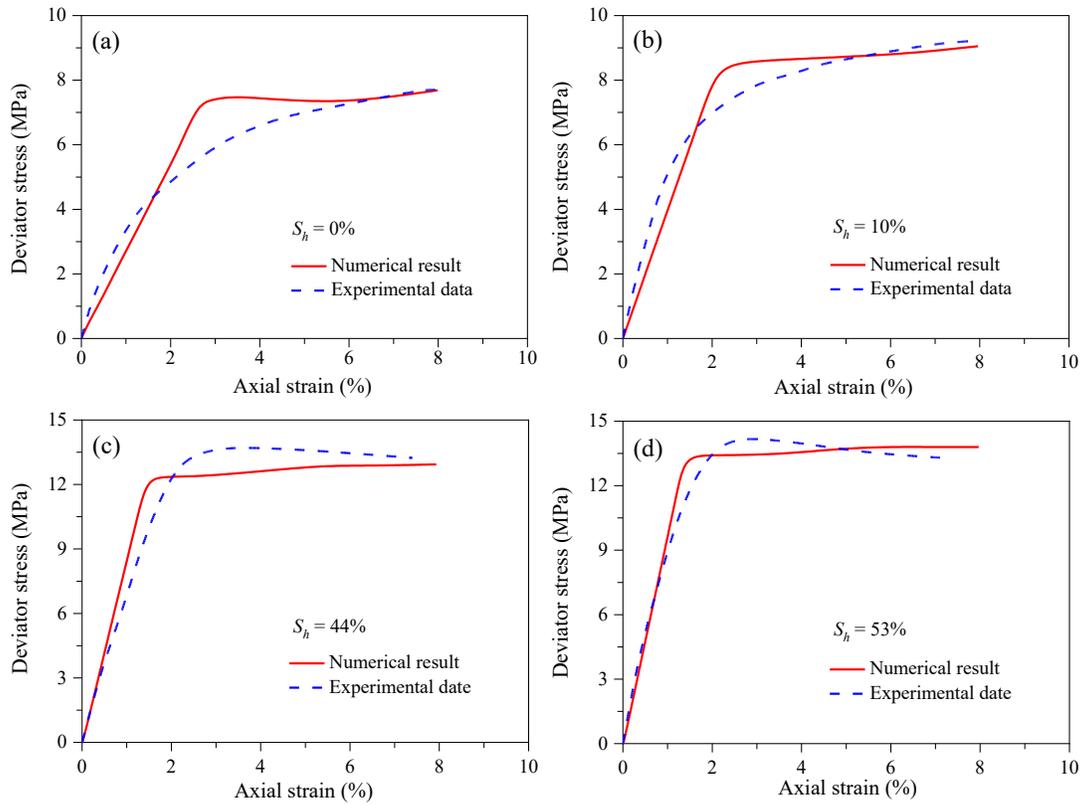
**Fig. 3**. Comparison between experimental and simulation data of NGH-bearing sediment triaxial test.

**Table 2**. Key parameters of sample (Ebinuma et al., 2005; Klar et al., 2005).

| Parameters | Values |
|---|---|
| Friction angle (°) | 34.6 |
| Cohesion (MPa) | 3.3 $S_h$ |
| Young's modulus (MPa) | 300 + 1350 $S_h$ |
| Poisson's ratio | 0.35 |
| Dilation angle (sin $\Psi$) | 0.45 $S_h$ |

were conducted by applying the proposed model. The stress-strain curves obtained by the experiment and simulation are displayed in Fig. 3. It can be observed that at high NGH saturation, the numerical curve fits well with the experimental curve, including the elastic and plastic deformation stages after yield. Elasticity deformation was considered in the proposed fluid–structure coupling model. Because the NGH saturation in subsequent simulations was relatively high, it can be considered that the proposed model performed well.

## 4. Numerical method

### 4.1 Computational model

In this study, an ideal NGH reservoir referencing the SH2 site in the Shenhu sea area was established. The geometric and physical properties of the reservoir were selected based on

**Table 3**. Key parameters of NGH reservoir model (Klar et al., 2010; Sun et al., 2019).

| Parameters | Value |
|---|---|
| Overburden thickness (m) | 28 |
| NGH sediment thickness (m) | 44 |
| Underburden thickness (m) | 28 |
| Wellbore radius (m) | 0.1 |
| Wellbore length (m) | 69 |
| Grain density (kg/m$^3$) | 2600 |
| Fluid density (kg/m$^3$) | 1040 |
| Fluid compressibility (Pa$^{-1}$) | $1 \times 10^{-8}$ |
| Fluid dynamic viscosity (Pa·s) | $1.01 \times 10^{-3}$ |
| Young's modulus (Pa) | $0.3 \times 10^{9*}$ $0.705 \times 10^{9**}$ $0.3 \times 10^{9***}$ |
| Poisson's ratio | 0.35 |
| Porosity | $0.42^*$ $0.40^{**}$ $0.38^{***}$ |
| Permeability (m$^2$) | $1 \times 10^{-14}$ |

Notes: * is overburden, ** is NGH sediment, *** is underburden.

**Fig. 4**. (a) Computing domain and (b) Meshing strategy.

previous studies (Klar et al., 2010; Sun et al., 2019). The computational domain comprised an overburden layer, stimulated reservoir volume (SRV), NGH layer enclosing the SRV, underburden layer, vertical production well, and horizontal slots constructed by WJS, as indicated in Fig. 4(a). The domain was a 100 m × 100 m × 100 m cube located at a depth of 1,392-1,492 m below the sea level. The SRV had a 40 m × 40 m × 30 m hexahedral volume and was located at the center of the NGH layer. The production well was located on the central axis of the computational domain. The slot was disc-shaped and centered on the wellbore axis. The key parameters are listed in Table 3.

### 4.2 Initial and boundary conditions

The initial and boundary conditions included two parts: the flow field and solid field. In the flow field, the reservoir was initially saturated with water. The initial pressure in the reservoir followed a hydrostatic distribution. The pressure

increased linearly from the top boundary 14.01 MPa to the bottom boundary 15.00 MPa. The side boundaries were set as the pressure boundaries, and the pressures were the same as the initial values. The inner wall surface of the slot was set as the pressure boundary, and the pressure was determined based on the liquid column pressure in the wellbore. For the solid field, the top boundary was set as the load boundary. The bottom boundary was set as the fixed constraint boundary. The side boundaries were set as specified displacement boundaries, with which displacement could only occur in the vertical direction. The slot inner walls were set as the free boundaries. According to the overlying weight, the top boundary load was set to 16.33 MPa.

### 4.3 Model meshing

The meshing scheme is displayed in Fig. 4(b). First, the top surface was discretized using triangular elements. The meshes were then swept from the top surface to the bottom surface.

**Table 4**. WJS scheme.

| Case | Pressure (MPa) | Radius (m) | Thickness (m) | Spacing (m) | Number |
|------|----------------|------------|---------------|-------------|--------|
| Single | 10.2, 11.5, 13.0, 14.6, 16.0 | 5 | 0.1 | - | 1 |
| | 14.6 | 5 | 0.05, 0.2 | - | 1 |
| Multiple | 10.2, 14.6 | 1, 3, 5, 7 | 0.1 | 5 | 3 |
| | | 5 | 0.1 | 2, 4, 6, 8, 10 | 3 |
| | | 5 | 0.1 | - | 3, 5, 7, 9 |

Consequently, triangular prismatic elements were generated in the domain. The meshes in the SRV region were refined to improve the calculation accuracy because this region was the key part where fluid flow and sediment deformation occur. To ensure that the simulation results were mesh-independent, the $z$-stress at a point near the slot for different mesh numbers was obtained and compared. The results indicated that a mesh number of approximately 131,262 was suitable for subsequent simulations, which balanced the computational time and precision. A segregated solution approach was employed to solve the partial differential equations. Absolute tolerance was regarded as the convergence criterion of the numerical solutions and was set to $10^{-5}$.

### 4.4 Slotting strategy

The slots were simplified to a disc shape; the geometric parameters were thickness $H_s$ and radius $R_s$. The slot arrangement along the wellbore was controlled by the spacing $D_s$ and number $N_s$. In addition, the fluid pressure acting on the slot inner wall $P_i$ could influence the flow and deformation. To clarify the reservoir response behavior and sensitivity of the parameters, the WJS scheme was designed and is presented in Table 4.

### 4.5 Analytical method

Because the model was axisymmetric, the $xz$ cross section in the SRV passing through the wellbore axis was selected as the analysis object. The pore pressure, stress, displacement, and volumetric fields on the $xz$ cross section were extracted to analyze the reservoir response behavior. To facilitate the discussion, two auxiliary lines were made on the $xz$ cross section. The horizontal auxiliary line was located in the middle of two adjacent slots. The vertical auxiliary line was located at a half-radius from the slot center. For the single-slot case, the horizontal auxiliary line was located above the slot, $0.5R_s$ away from the slot upper wall. The maximum stress change, maximum displacement, and maximum volume strain on the auxiliary lines were taken out for quantitative comparative analysis. The stress change ($\Delta\sigma_d$) indicates the change in the effective stress before and after slotting, and is expressed as:

$$\Delta\sigma_d = \sigma_a - \sigma_b \tag{12}$$

where $\sigma_b$ is the in-situ stress in the reservoir matrix and $\sigma_a$ is the stress in the reservoir matrix after the WJS disturbance. In addition, the WJS disturbance range $R_d$ was defined; this

indicates the distance from the farthest reservoir location disturbed by the WJS to the production wellbore. The farthest reservoir disturbance location was determined by the stress-change rate $\gamma$, which is given by:

$$\gamma = \left| \frac{\sigma_a - \sigma_b}{\sigma_b} \right| \times 100\% \tag{13}$$

The effective disturbance was considered to occur when $\gamma$ was not less than 10%. That is, $\gamma$ at the effective disturbance boundary was equal to 10%. The distance from the effect disturbance boundary to the wellbore was regarded as the disturbance range, $R_d$.

## 5. Results and discussion

### 5.1 Single-slot case

As the slot is in a horizontal disk shape, the calculation indicates that the vertical disturbance is more apparent than the horizontal disturbance. Hence, the follow-up analysis mainly focuses on the vertical direction, that is, the $z$-axis direction. For the stress, displacement, and volumetric strain, positive values represent tension, positive $z$-axis direction, and expansion, respectively.

Fig. 5(a) displays the reservoir field evolution induced by a single slot. It can be observed that when $P_i$ is equal to the reservoir pore pressure near slot $P_r = 14.6$ MPa, that is, a balanced state, the $P_r$ field is hardly disturbed. When $P_i = 16.0$ MPa $> P_r$, the fluid in the slot invades the reservoir, leading to a $P_r$ distribution that decreases from the near-slot region to the deep reservoir. Conversely, when $P_i = 10.2, 11.5$, and $13.0$ MPa $< P_r$, the reservoir fluid flows into the slot, forming a $P_r$ distribution that reduces from the deep reservoir towards the slot. As can be observed from the stress contours in Fig. 5(a), the slot can reduce the in-situ compressive stress in the adjacent region and even transform it into tensile stress. This is because the slot wall loses the original sediment skeleton support and the fluid in the slot cannot generate sufficient support. The sediment then tends to move into the slot space, as indicated in the displacement contours. Furthermore, with an increase in $P_i$, the disturbances in the stress and displacement weaken, whereas the volumetric strain disturbance strengthens. This could be because the increase in $P_i$ enhances the support to the slot wall whereas the resulted increase of pore pressure reduces the volumetric part stress in the matrix skeleton, as characterized by Eq. (2).

Fig. 5(b) plots the stress change rate contour maps in
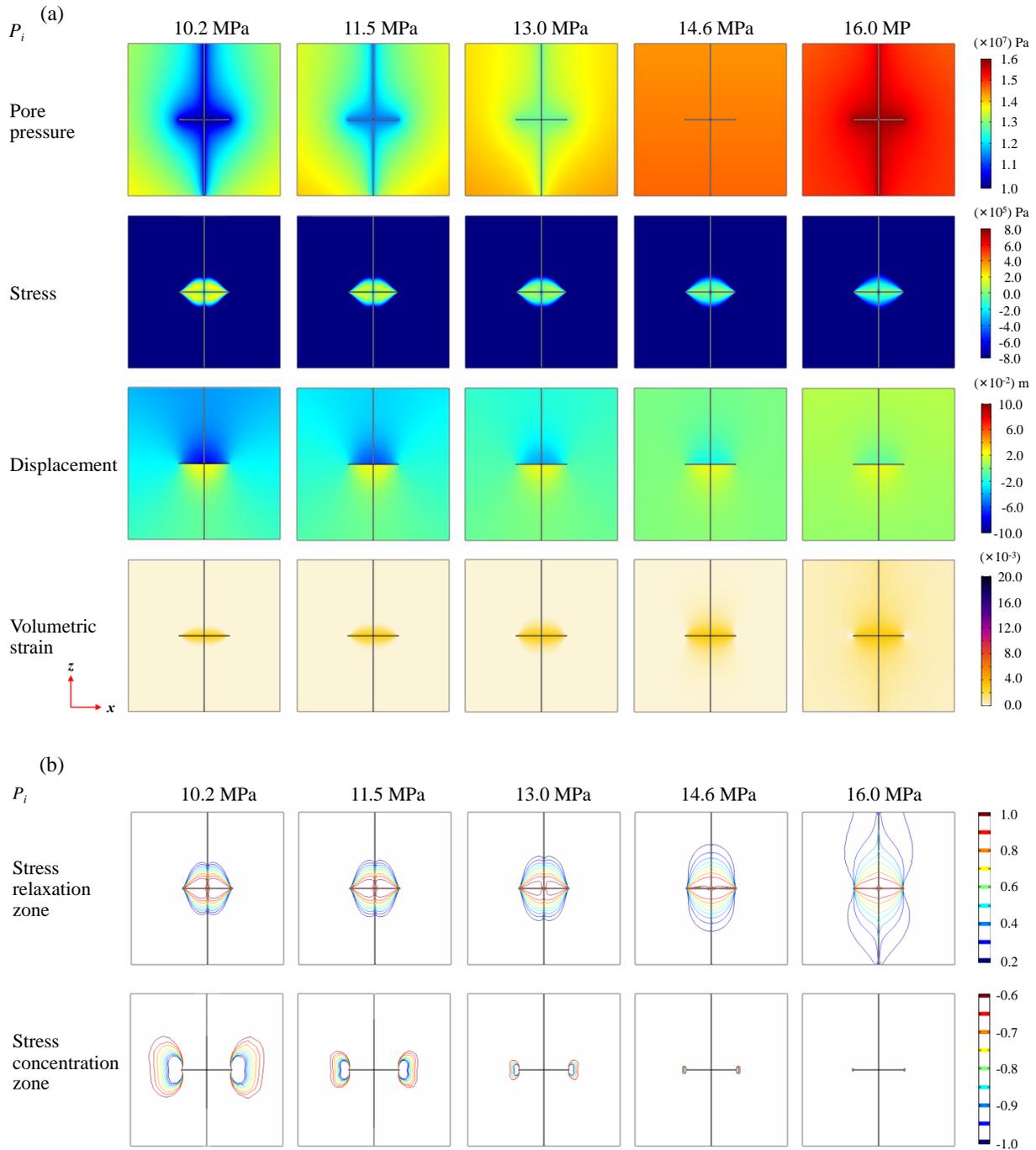
**Fig. 5**. Under different $P_i$ in single-slot case: (a) reservoir field disturbance and (b) stress change rate.

the single-slot case. A positive stress change rate means the compressive stress decreased or the tensile stress increased, and vice versa. It can be observed that the slot disturbance can induce not only stress relaxation, but also stress concentration. The stress relaxation zone is mainly distributed on the upper and lower sides of the slot, whereas the stress concentration region is mainly formed around the slot circumference. In addition, as $P_i$ increases, the stress relaxation zone tends to expand whereas the stress concentration region shrinks. This is related to the relationship between the pore pressure

and effective stress in porous media. Fig. 6 depicts a partial enlarged view of the slot wall deformation under different $P_i$. The slot walls are deformed inward under the surrounding sediment extrusion. The increasing $P_i$ can enhance the load exerted by the fluid on the slot wall, and consequently weaken the deformation of the slot wall. This is consistent with the stress and displacement cloud pictures in Fig. 5(a).

Fig. 7 displays the maximum horizontal and vertical disturbance ranges for different $P_i$ values. It can be observed that when $P_i < 16$ MPa, with increasing $P_i$, the horizontal influen-
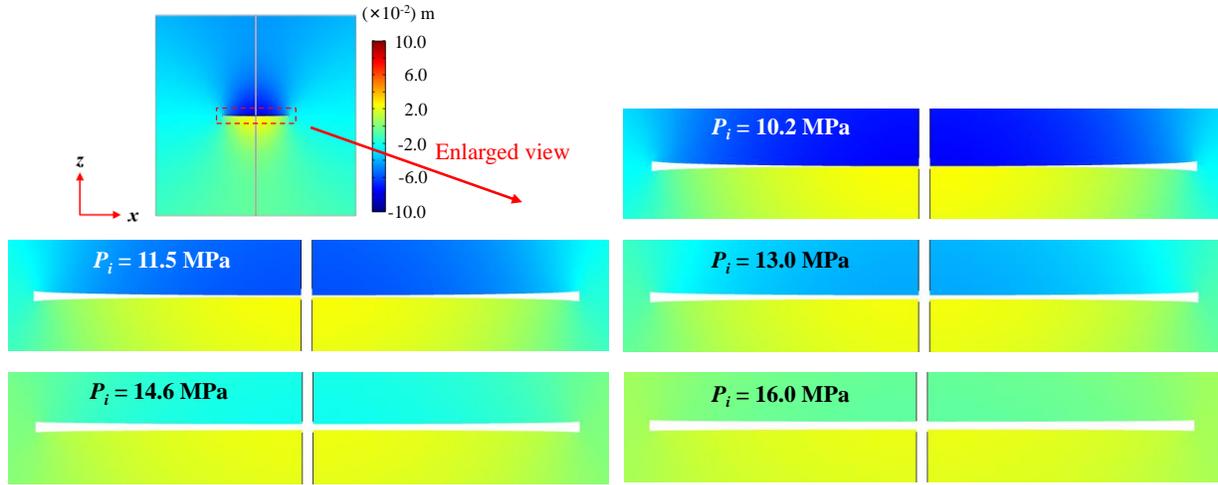
**Fig. 6**. Partial enlarged view of slot wall deformation under different $P_i$ in single-slot case.
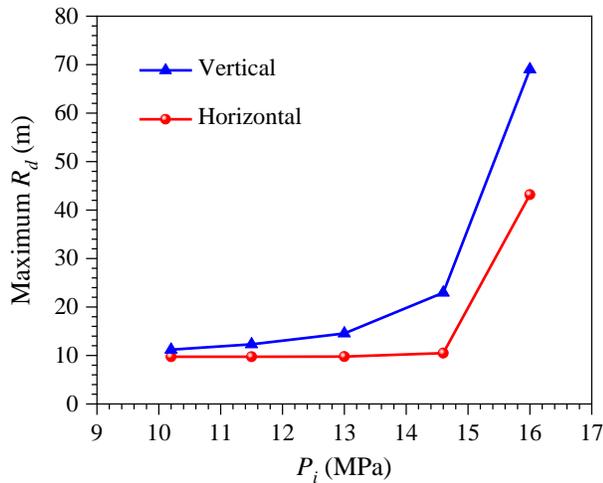


**Fig. 7**. Disturbance range under different $P_i$ in single-slot case.

ce range is virtually unchanged, close to the slot diameter, whereas the vertical influence range increases. When $P_i = P_r = 14.6$ MPa, the vertical influence range exceeds 20 m. At $P_i = 16$ MPa, the influence range increases significantly, which is likely caused by the high transmission efficiency and large pore pressure propagation range.

Fig. 8 illustrates the distribution of the mechanical parameters on the auxiliary lines. On the horizontal auxiliary line, the maximum changes of stress, displacement, and volumetric strain are 2.51, 2.48, 2.44, 2.41, and 2.40 MPa; $6.54 \times 10^{-2}$, $5.11 \times 10^{-2}$, $3.46 \times 10^{-2}$, $1.65 \times 10^{-2}$, and $0.16 \times 10^{-2}$ m; $0.30 \times 10^{-3}$, $0.21 \times 10^{-3}$, $0.80 \times 10^{-3}$, $1.49 \times 10^{-3}$, and $2.14 \times 10^{-3}$, for $P_i = 10.2$, 11.5, 13.0, 14.6, and 16.0 MPa, respectively. On the vertical auxiliary line, the maximum changes of stress, displacement, and volumetric strain are 3.01, 2.95, 2.87, 2.813, and 2.810 MPa; $6.87 \times 10^{-2}$, $5.43 \times 10^{-2}$, $3.78 \times 10^{-2}$, $1.96 \times 10^{-2}$, and $1.95 \times 10^{-2}$ m; $3.06 \times 10^{-3}$, $3.09 \times 10^{-3}$, $3.13 \times 10^{-3}$, $3.17 \times 10^{-3}$, and $3.21 \times 10^{-3}$, for $P_i = 10.2$, 11.5, 13.0, 14.6, and 16.0 MPa, respectively. This implies that with a decrease in $P_i$, the maximum changes of stress and displacement on the horizontal and vertical

auxiliary lines increase, indicating the slot disturbance to the surrounding sediment is enhanced. It should also be noted that decreasing $P_i$ leads to a reduced volumetric strain, which is related to the increase in effective stress in the sediment skeleton.

### 5.2 Effects of slotting parameters on reservoir disturbance at balanced pressure

To obtain a superior WJS reservoir reconstruction effect, the reservoir response behavior under different $H_s$, $R_s$, $D_s$, and $N_s$ were studied and analyzed. A balanced pressure condition means $P_i = P_r$, which is the bottom-hole pressure condition when constructing slots.

#### 5.2.1 Effect of slot thickness

The slot deformation at $H_s = 0.05$, 0.10, and 0.20 m is analyzed. It can be found that at $H_s = 0.05$ m, the wall displacement does not close the slot. With the increase in $H_s$, the slot wall deformation has no clear change because the force situation is virtually unchanged, which can be verified from practically the same displacement distribution and maximum stress on the vertical auxiliary line with different $H_s$. This indicates that when $H_s$ is greater than the total displacement of the upper and lower walls, under the same force situation, a small change in $H_s$ has minimal effect on the disturbance to the surrounding sediment. Hence, in the follow-up study, $H_s$ was set constant at 0.10 m. It should be noted that if there is no support from the fluid inside the slot, the slot wall could collapse, that is, the increase in $H_s$ in this case could strengthen the disturbance.

#### 5.2.2 Effect of slot radius

For simplicity, the cloud pictures of the reservoir field disturbance and stress change rate similar to those in Fig. 5 are not drawn in Sections 5.2.2, 5.2.3, and 5.2.4. It can be found that with an increase in $R_s$, the reservoir-disturbed region is clearly enlarged, not only in the horizontal direction, but also in the vertical direction. At $R_s = 1$ m, the disturbance
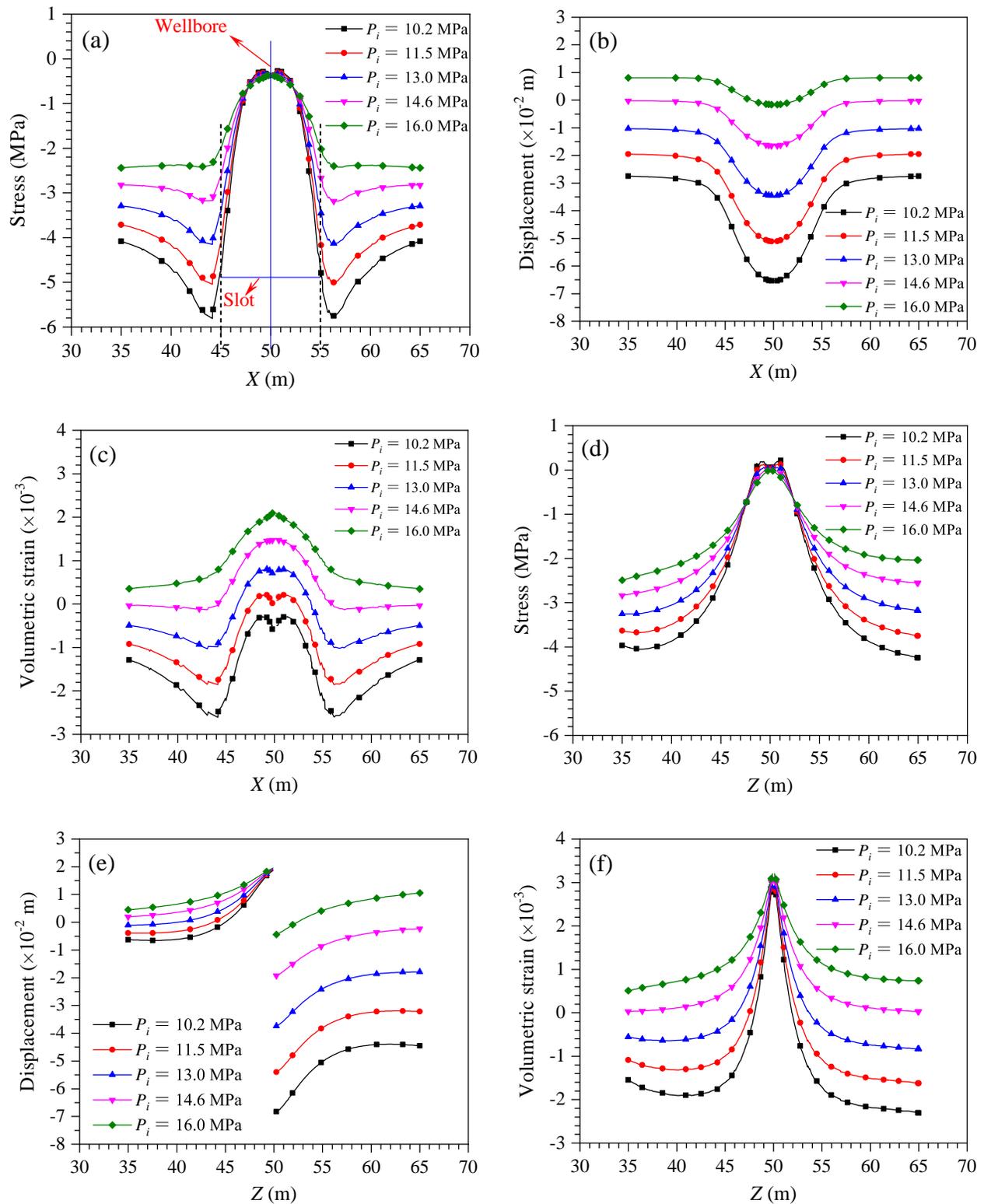
**Fig. 8**. Stress, displacement, and volumetric strain distributions on horizontal auxiliary line (a), (b), and (c), and vertical auxiliary line (d), (e), and (f).
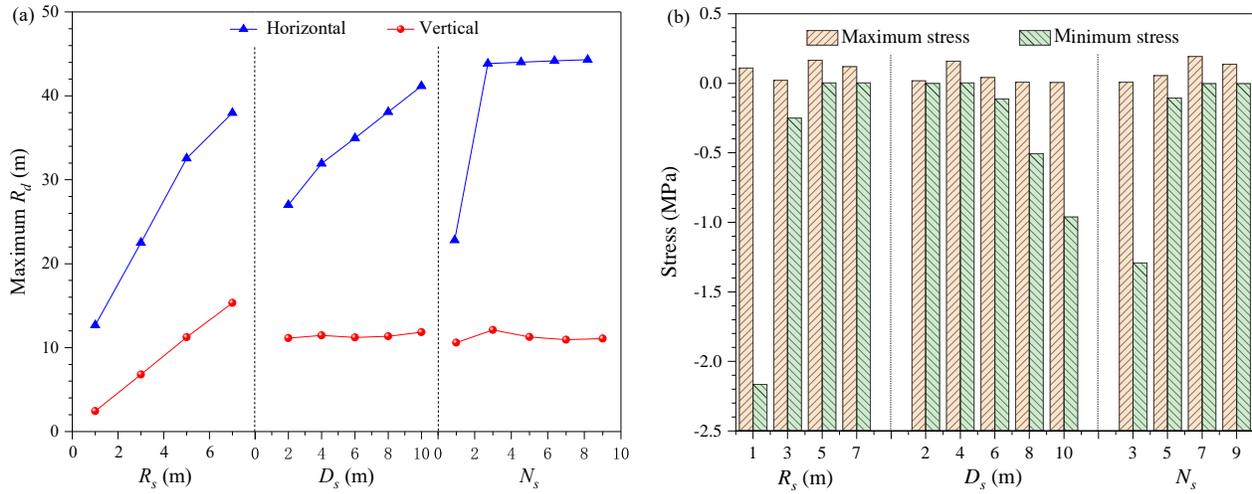
**Fig. 9**. Under different $R_s$, $D_s$ and $N_s$: (a) disturbance range and (b) maximum and minimum stresses on vertical auxiliary line.

between the slots is not evident. With an increasing $R_s$, the disturbance between the slots becomes remarkable. In addition, the displacements in the uppermost and bottommost parts of the slots are more notable than those between the slots. This could be because the sediment between the slots has upward and downward displacement trends at the same time, leading to a counteracting effect. However, the stress and volumetric strain distributions indicate that there is an acceptable sediment-loosening effect between the slots, possibly due to a superimposed effect. The stress reduction and concentration zones expand with an increase of $R_s$. The stress concentration zone is characterized by multiple separate blocks under small $R_s$ and as a whole under large $R_s$. The stress concentration is not conducive to improving sediment permeability. Nonetheless, the subsequent depressurization extraction process also causes a compaction effect. The stress concentration here could reduce the compaction trend in advance.

Fig. 9(a) displays the slot disturbance range of the three-slot case under different $R_s$. The horizontal disturbance range is virtually equal to $R_s$. The vertical disturbance range increases clearly with the increase of $R_s$, although the slots only change in horizontal parameter $R_s$. At $R_s = 1$ m, the vertical influence range is approximately 13 m, whereas at $R_s = 7$, the vertical influence range rapidly increases to approximately 38 m. Fig. 9(b) displays the maximum and minimum stresses on the vertical auxiliary line under different $R_s$. As $R_s$ increases, the maximum stress is virtually constant and the minimum stress increases. After $R_s \geqslant 3$ m, the minimum stress increases marginally. This indicates that with the increase of $R_s$, the loosening effect in the sediment between the slots is enhanced; however, the enhanced effect tends to weaken.

### 5.2.3 Effect of slot spacing

In terms of the effect of the slotting spacing, as $D_s$ increases, the influence region of the individual slot gradually changes from overlapping to separating. The separation of the slot influence region weakens the superimposed effect in the stress and volumetric strain disturbances, and the offset effect

in the displacement disturbance between the slots. Furthermore, with increasing $D_s$, the stress reduction zone is enlarged in the vertical direction. The stress concentration zone presents as a whole at small $D_s$ and is characterized by separated small blocks at large $D_s$. In addition, as indicated in Fig. 9, as $D_s$ increases from 2 to 10 m, the vertical influence range increases from 27 to 41 m, whereas the horizontal influence range changes little. The maximum stress changes marginally, and the minimum stress decreases significantly with the increase in $D_s$, which indicates that the loosening effect between the slots gradually weakens and becomes heterogeneous.

### 5.2.4 Effect of slot number

For the effect of the slotting number, as $N_s$ increases, the disturbance areas of the individual slots gradually overlap. The stress and volumetric disturbances around the wellbore become uniform. The offset effect of the displacement between the slots becomes clear. The stress concentration zones of the individual slots appear to shrink, particularly in the middle slots. Furthermore, the vertical-influence range of multiple slots is larger than that of a single slot. However, when multiple slots are arranged at equal intervals in a limited wellbore depth range, $N_s$ has only a minimal effect on the vertical influence range, as indicated in Fig. 9(a). As displayed in Fig. 9(b), with increasing $N_s$, the maximum stress changes marginally, whereas the minimum stress increases significantly at first and then only marginally. This indicates that an excessive number of slots does not further enhance the loosening effect between the slots. Under the conditions here, $N_s = 5$ is appropriate because increasing $N_s$ further does not only have no clear gain effect, but also increases the construction cost and risk.

### 5.3 Reservoir response behavior at underbalanced pressure

To analyze the slot disturbance to a reservoir under a wellbore depressurization condition, the reservoir disturbance fields at underbalanced pressure $P_i = 10.2$ MPa $< P_r = 14.6$ MPa were studied and compared with those under a balanced
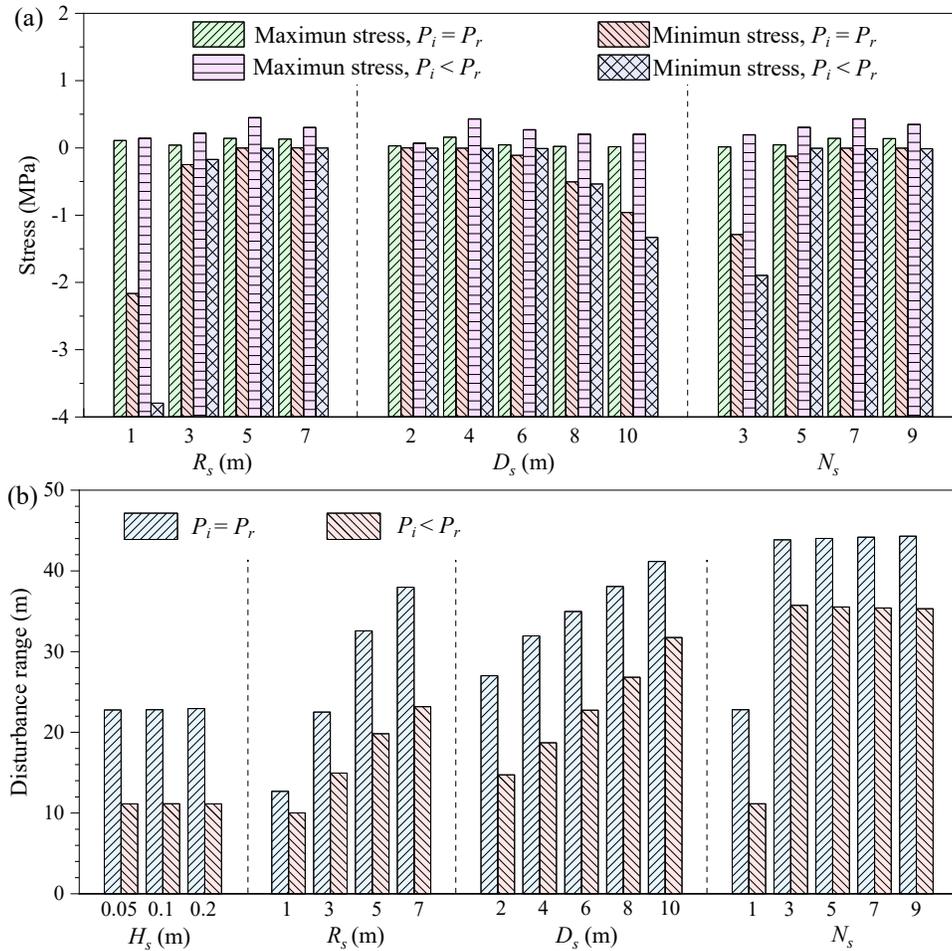
**Fig. 10**. Comparison under $P_i = P_r$ and $P_i < P_r$. (a) Maximum and minimum stresses on vertical auxiliary line and (b) disturbance range.

pressure $P_i = P_r$ = 14.6 MPa. The maximum and minimum stresses on the vertical auxiliary line, as well as the vertical disturbance range under the two bottom-hole pressure conditions, are illustrated in Fig. 10.

It can be observed from Fig. 10(a) that the influence of the slotting parameters on the reservoir response behavior at $P_i < P_r$ is similar to that at $P_i = P_r$. In addition, the maximum stresses on the vertical auxiliary line at $P_i < P_r$ are marginally greater than those at $P_i = P_r$, whereas the minimum stresses on the vertical auxiliary line at $P_i < P_r$ are near those at $P_i = P_r$, except for the cases of $R_s = 1$, $D_s = 10$, and $N_s = 3$. This indicates that the stress relaxation effect between the slots at $P_i < P_r$ is superior to that at $P_i = P_r$ under the majority of slotting parameters, which is likely because of the lower fluid pressure load on the slot wall at $P_i < P_r$. For $R_s = 1$, $D_s = 10$, and $N_s = 3$, the disturbance regions of the individual slots are far apart, and the stress relaxation caused by slot wall deformation is weak in the middle of two adjacent slots. However, low pore pressure continues to cause a similar compaction effect. The combination of these two aspects results in the weakening of the stress relaxation effect between the slots at $P_i < P_r$. As indicated in Fig. 10(b), the disturbance

ranges in the vertical direction at $P_i < P_r$ are smaller than those at $P_i = P_r$. This could be because at a position away from the slots, the stress relaxation induced by the slots is weakened by the compaction effect caused by the low pore pressure.

## 6. Conclusions

In this study, a reservoir reconstruction method of NGH sediment disturbance induced by WJS was proposed. The sediment disturbance mechanism near the slots was analyzed using a 3D flow-structure coupling model. Geological background referenced the SH2 site in the Shenhu sea area of the SCS. Horizontal slots along the vertical well mode were adopted. The key findings of this study are as follows.

1) Distinct disturbance zones were formed around the slots, which could be divided into two types. One was the stress relaxation zone, and the other was the stress concentration zone.

2) The fluid pressure inside slot significantly influenced the reservoir response behavior. With its increase, the stress relaxation effect weakened. The volumetric expansion strain was enhanced.

3) A small change in $H_s$ had minimal effect on the disturbance to the surrounding sediment. With the increase of $R_s$, the horizontal and vertical disturbance ranges were enlarged.

4) As $D_s$ increased, the vertical disturbance range increased. The stress and volumetric strain disturbances between the slots weakened, whereas the displacement disturbance increased.

5) With an increasing $N_s$ the stress disturbance between the slots tended to be strengthened and uniform. After exceeding five, a further increase in $N_s$ had a minimal effect on improving the sediment loosening.

6) Compared with $P_i = P_r$, at $P_i < P_r$, the stress relaxation effect between the slots was improved under the majority of the slotting parameters; however, the disturbance range was smaller.

7) It should be noted that the conclusions are based on the assumption that the reservoir was saturated with single-phase water and the influence of hydrate decomposition and formation was not considered. This condition was relatively consistent with the reservoir state before exploitation, and the disturbance of WJS to the primary reservoir before exploitation could be analyzed. In the exploitation process, the decomposition and formation of hydrates and multiphase flow in pores have a significant influence on the formation of the mechanical state and seepage field. Hence, the effect of WJS on the reservoir mechanics and seepage during exploitation will be studied in future work.

## Acknowledgements

## Conflict of interest

The authors declare no competing interest.

## References

Biot, M. A. Mechanics of deformation and acoustic propagation in porous media. Journal of Applied Physics, 1962, 33(4): 1482-1498.

Cai, J., Xia, Y., Lu, C., et al. Creeping microstructure and fractal permeability model of natural gas hydrate reservoir. Marine and Petroleum Geology, 2020a, 115: 104282.

Cai, J., Xia, Y., Xu, S., et al. Advances in multiphase seepage characteristics of natural gas hydrate sediments. Chinese Journal of Theoretical and Applied Mechanics, 2020b, 52(1): 208-223. (in Chinese)

Chen, L., Feng, Y., Okajima, J., et al. Production behavior and numerical analysis for 2017 methane hydrate extraction test of Shenhu, South China Sea. Journal of Natural Gas Science and Engineering, 2018, 53: 55-66.

Chen, C., Yang, L., Jia, R., et al. Simulation study on the effect of fracturing technology on the production efficiency of natural gas hydrate. Energies, 2017, 10(8): 1241.

Cui, Y., Lu, C., Wu, M., et al. Review of exploration and production technology of natural gas hydrate. Advances in Geo-Energy Research, 2018, 2(1): 53-62.

Ebinuma, T., Kamata, Y., Minagawa, H., et al. Mechanical properties of sandy sediment containing methane hydrate. Paper Presented at Proceedings of $5^{th}$ International Conference on Gas Hydrate, Trondheim, Norway, 12-16 June, 2005.

Feng, Y., Chen, L., Kanda, Y., et al. Numerical analysis of gas production from large-scale methane hydrate sediments with fractures. Energy, 2021, 236: 121485.

Feng, Y., Chen, L., Suzuki, A., et al. Enhancement of gas production from methane hydrate reservoirs by the combination of hydraulic fracturing and depressurization method. Energy Conversion and Management, 2019, 184: 194-204.

Feng, C., Li, S. H., Wang, L. X. A numerical method to solve pore seepage problems based on element local coordinate system. Rock & Soil Mechanics, 2014, 35(2): 584-590. (in Chinese)

Guo, W., Zhang, P., Wang, Y., et al. Evolution on the gas production from low permeability gas hydrate reservoirs by depressurization combined with reservoir stimulation. Energy & Fuels, 2020, 34 (12): 15819-15828.

Ito, T., Igarashi, A., Suzuki, K., et al. Laboratory study of hydraulic fracturing behavior in unconsolidated sands for methane hydrate production. Paper OTC 19324 Presented at the Offshore Technology Conference, Houston, Texas, USA, 5-8 May, 2008.

Ju, X., Liu, F., Fu, P., et al. Gas production from hot water circulation through hydraulic fractures in methane hydrate-bearing sediments: THC-coupled simulation of production mechanisms. Energy & Fuels, 2020, 34(4): 4448-4465.

Khodaverdian, M., Mcelfresh, P. Hydraulic fracturing stimulation in poorly consolidated sand: mechanisms and consequences. Paper SPE 63233 Presented at the SPE Annual Technical Conference and Exhibition, Texas, USA, 1-4 October, 2000.

Klar, A., Soga, K. Coupled deformation-flow analysis for methane hydrate production by depressurized wells. Paper Presented at $3^{rd}$ International Biot Conference on Poromechanics, Oklahoma, USA, 25-27 May, 2005.

Klar, A., Soga, K., Ng, M. Coupled deformation-flow analysis for methane hydrate extraction. Geotechnique, 2010, 60(10): 765-776.

Konno, Y., Jin, A. Y., Yoneda, A. J., et al. Hydraulic fracturing in methane-hydrate-bearing sand. RSC Advances, 2016, 6(77): 73148-73155.

Kurihara, M., Sato, A., Funatsu, K., et al. Analysis of production data for 2007/2008 Mallik gas hydrate production tests in Canada. Paper SPE 132155 Presented at the International Oil and Gas Conference and Exhibition in

China, Beijing, China, 8-10 June, 2010.

Li, Y., Liu, L., Jin, Y., et al. Characterization and development of natural gas hydrate in marine clayey-silt reservoirs: A review and discussion. Advances in Geo-Energy Research, 2021a, 5(1): 75-86.

Li, B., Ma, X., Zhang, G., et al. Enhancement of gas production from natural gas hydrate reservoir by reservoir stimulation with the stratification split grouting foam mortar method. Journal of Natural Gas Science and Engineering, 2020a, 81: 103473.

Li, Z., Wan, T., Liang, Q. The influence of reservoir reconstruction on the production capacity of natural gas hydrate. Ground Water, 2020b, 42(3): 120-124. (in Chinese)

Li, S., Wu, D., Wang, X., et al. Enhanced gas production from marine hydrate reservoirs by hydraulic fracturing assisted with sealing burdens. Energy, 2021b, 232: 120889.

Liang, Y., Tan, Y., Luo, Y., et al. Progress and challenges on gas production from natural gas hydrate-bearing sediment. Journal of Cleaner Production, 2020, 261: 121061.

Liu, J., Li, X. Recent advances on natural gas hydrate exploration and development in the South China Sea. Energy & Fuels, 2021, 35(9): 7528-7552.

Liu, L., Lu, X., Zhang, X., et al. Numerical simulations for analyzing deformation characteristics of hydrate-bearing sediments during depressurization. Advances in Geo-Energy Research, 2017, 1(3): 135-147.

Lu, C., Qin, X., Mao, W., et al. Experimental study on the propagation characteristics of hydraulic fracture in clayey-silt sediments. Geofluids, 2021: 6698649.

Ma, X., Cheng, J., Sun, Y., et al. 2D Numerical simulation of hydraulic fracturing in hydrate-bearing sediments based on the cohesive element. Energy & Fuels, 2021a, 35(5): 3825-3840.

Ma, X., Sun, Y., Guo, W., et al. Numerical simulation of horizontal well hydraulic fracturing technology for gas production from hydrate reservoir. Applied Ocean Research, 2021b, 112: 102674.

Makogon, Y. F. A gas hydrate formation in the gas saturated layers under low temperature. Gas Industry, 1965, 5: 14-15.

Makogon, Y. F. Natural gas hydrates-A promising source of energy. Journal of Natural Gas Science and Engineering, 2010, 2(1): 49-59.

Masuda, Y., Konno, Y., Iwama, H., et al. Improvement of near wellbore permeability by methanol stimulation in a methane hydrate production well. Paper OTC 19433 Presented at the Offshore Technology Conference, Houston, Texas, USA, 5-8 May, 2008.

Shaibu, R., Sambo, C., Guo, B., et al. An assessment of methane gas production from natural gas hydrates: Challenges, technology and market outlook. Advances in Geo-Energy Research, 2021, 5(3): 318-332.

Shen, P., Li, G., Li, X., et al. Application of fracturing technology to increase gas production in low-permeability hydrate reservoir: A numerical study. Chinese Journal of Chemical Engineering, 2021, 34: 267-277.

Sun, Y., Li, S., Lu, C., et al. The characteristics and its implications of hydraulic fracturing in hydrate-bearing clayey silt. Journal of Natural Gas Science and Engineering, 2021, 95: 104189.

Sun, J., Ning, F., Liu, T., et al. Gas production from a silty hydrate reservoir in the South China Sea using hydraulic fracturing: A numerical simulation. Energy Science & Engineering, 2019, 7(4): 1106-1122.

Terzaghi, K. Theoretical Soil Mechanics. New York, USA, John Wiley & Sons, 1943.

Too, J. L., Cheng, A., Khoo, B. C., et al. Hydraulic fracturing in a penny-shaped crack. Part I: Methodology and testing of frozen sand. Journal of Natural Gas Science and Engineering, 2018a, 52: 609-618.

Too, J. L., Cheng, A., Khoo, B. C., et al. Hydraulic fracturing in a penny-shaped crack. Part II: Testing the frackability of methane hydrate-bearing sand. Journal of Natural Gas Science and Engineering, 2018b, 52: 619-628.

Truesdell, C. The Linear Theory of Elasticity in the Encyclopedia of Physics. Berlin, Springer-Verlag, 1972.

Wanniarachchi, W., Ranjith, P., Perera, M. Shale gas fracturing using foam-based fracturing fluid: a review. Environmental Earth Sciences, 2017, 76(2): 91.

Wu, N., Li, Y., Wan, Y., et al. Prospect of marine natural gas hydrate stimulation theory and technology system. Natural Gas Industry B, 2021, 8(2): 173-187.

Wu, S., Liu, J., Xu, H., et al. Application of frequency division inversion in the prediction of heterogeneous natural gas hydrates reservoirs in the Shenhu Area, South China Sea. China Geology, 2022, 5: 251-266.

Yamamoto, K., Terao, Y., Fujii, T., et al. Operational overview of the first offshore production test of methane hydrates in the Eastern Nankai Trough. Paper OTC 25243 Presented at the Offshore Technology Conference, Texas, USA, 5-8 May, 2014.

Yamamoto, K., Wang, X., Tamaki, M., et al. The second offshore production of methane hydrate in the Nankai Trough and gas production behavior from a heterogeneous methane hydrate reservoir. RSC Advances, 2019, 9(45): 25987-26013.

Yang, Y., He, Y., Zheng, Q. An analysis of the key safety technologies for natural gas hydrate exploitation. Advances in Geo-Energy Research, 2017, 1(2): 100-104.

Yang, L., Shi, F., Yang, J. Experimental studies on hydraulic fracturing in hydrate sediment. Chemistry and Technology of Fuels and Oils, 2020, 56(1): 107-114.

Yao, Y., Guo, Z., Zeng, J., et al. Discrete element analysis of hydraulic fracturing of methane hydrate-bearing sediments. Energy & Fuels, 2021, 35(8): 6644-6657.

Ye, J., Qin, X., Xie, W., et al. The second natural gas hydrate production test in the South China Sea. China Geology, 2020, 3: 197-209.

Yin, Z., Linga, P. Methane hydrates: A future clean energy resource. Chinese Journal of Chemical Engineering, 2019, 27(9): 36-46.

Yu, T., Guan, G., Wang, D., et al. Gas production enhancement from a multilayered hydrate reservoir in the South China Sea by hydraulic fracturing. Energy & Fuels, 2021, 35(15): 12104-12118.

Yuan, Y., Xu, T., Xin, X., et al. Enhanced gas production from

clayey-silt hydrate reservoirs based on near-well reservoir reconstruction using the high-pressure jet grouting technology. Journal of Natural Gas Science and Engineering, 2021, 94: 104121.

Yun, Q., Youhong, S., Bing, L. Numerical simulation study on the influence of near-well reservoir reconstruction on the depressurization and production characteristics of natural gas hydrate reservoirs. Drilling Engineering, 2021, 48(4): 85-96. (in Chinese)

Zhang, W., Shi, X., Jiang, S., et al. Experimental study of hydraulic fracture initiation and propagation in highly saturated methane-hydrate-bearing sands. Journal of Natural Gas Science and Engineering, 2020, 79(77): 103338.

Zhao, J., Xu, L., Guo, X., et al. Enhancing the gas production efficiency of depressurization-induced methane hydrate exploitation via fracturing. Fuel, 2021, 288: 119740.

Zhong, X., Pan, D., Zhai, L., et al. Evaluation of the gas production enhancement effect of hydraulic fracturing on combining depressurization with thermal stimulation from challenging ocean hydrate reservoirs. Journal of Natural Gas Science and Engineering, 2020, 83: 103621.

Zhong, X., Pan, D., Zhu, Y., et al. Fracture network stimulation effect on hydrate development by depressurization combined with thermal stimulation using injection-production well patterns. Energy, 2021, 228: 120601.

Zhou, S., Zhao, J., Li, Q., et al. Optimal design of the engineering parameters for the first global trial production of marine natural gas hydrates through solid fluidization. Natural Gas Industry B, 2018, 5(2): 118-131.